High Plasticity of an Iron Aluminide-based Material at Low Temperatures

V. Šíma[1*], P. Minárik[1], M. Cieslar[1], R. Král[1], P. Málek[1],
T. Chráska[2], F. Lukáč[2], H. Seiner[3], F. Průša[4]

[1]*Faculty of Math. & Phys., Charles University, Ke Karlovu 5, Praha 2, CZ-12116, Czech Rep.*
[2]*Institute of Plasma Physics AS CR, Za Slovankou 1782/3, Praha 8, CZ-18200, Czech Rep.*
[3]*Institute of Thermomechanics AS CR, Dolejškova 5, Praha 8, CZ-18200, Czech Rep.*
[4] *Dept. of Metals and Corrosion Eng., UCT Prague, Technická 5, Praha 6, CZ -16628, Czech Rep.*

.

ABSTRACT

Aims: To compare surprisingly high plasticity in compression at low temperature of high-quality compacts prepared by spark plasma sintering from atomized Fe-30.8Al-0.35Zr-0.11B (at.%) powder with tensile tests at the same conditions.

Study design: Compressive tests and tensile tests at room temperature and at 77 K, scanning and transmission electron microscopy, measurements of Young's and shear moduli data of the sintered material from room temperature to 80 K.

Place and Duration of Study: Faculty of Mathematics and Physics, Institute of Plasma Physics, Institute of Thermomechanics, Department of Metals and Corrosion Engineering, between October 2015 and November 2017.

Methodology: The feedstock powder was prepared using atomization in argon and consolidated by spark plasma sintering method. The microstructure and phase composition of the sintered samples were characterized by X-ray diffraction (XRD), scanning electron microscopy (SEM) with electron backscatter diffraction (EBSD) and by transmission electron microscopy (TEM). Mechanical properties of the feedstock powder were characterized by microhardness data, the compacts were in addition tested in compression and in tension. The elastic properties (Young's and shear moduli) of the examined material were measured by a combination of two ultrasonic methods: the pulse-echo method and the resonant ultrasound spectroscopy.

Results: High plasticity (plastic strain more than 30% without failure) was observed in compressive tests at room temperature and at 77 K. Electron microscopy observations revealed the dominating role of dislocation motion in compression at low temperatures. The ductility measured at tensile tests, on the other hand, was only about 1% with a typical brittle failure.

Conclusion: The TEM observations confirm that dislocations enable the plastic flow in compression at low temperatures. The poor ductility in tension is not an intrinsic behavior of the alloy, but it results from the nucleation and opening of nano/microcracks between sintered powder particles and/or cavities in partly hollow atomized particles.

Keywords: Intermetallics; Powder metallurgy; Mechanical properties; Scanning electron microscopy; Transmission electron microscopy.

* Tel.: +420 2 21911362;
E-mail address: sima@met.mff.cuni.cz.

1. INTRODUCTION

Iron aluminides based on FeAl and Fe_3Al have been widely studied, mainly because of their excellent high temperature oxidation and corrosion properties. However, poor formability and ductility, particularly at room temperature, present a serious problem for the industrial application of these materials. There are many factors influencing the plasticity of these materials (e.g. testing environment, Al content, substitutional alloying, dispersed particles, grain size, quenched-in vacancies) [1-5].

Spark plasma sintering (SPS) is a rapid powder consolidation technique that uses uniaxial pressure and heat generated by pulsed direct electric current. Powder densification can be achieved at significantly lower temperatures and shorter times by SPS than by conventional sintering thereby limiting grain growth and preserving the fine microstructure in the SPS consolidated samples [6].

The SPS procedure is often used to sinter powder prepared by mechanical alloying of elemental powders or by milling. Both the milling and the mechanical alloying are used to achieve mechanical activation of particle surfaces and grain refinement. SPS is also used for powders prepared by gas atomization of an alloy under argon. In both cases the milled powder is highly reactive with a heavily deformed microstructure. Sintering of such powders usually leads to a bulk material with improved hardness and strength [7].

The previous studies confirmed the advantages of the SPS-method by successful fabrication of dense fine-grained Fe-Al materials with promising mechanical properties [7-10].

In our previous unpublished work, cryo-milling of an atomized powder of an iron aluminide-based alloy was performed in liquid nitrogen at 77 K. The microstructure of powder particles before and after milling was compared. We observed clear signs of high intrinsic plasticity of the milled polycrystalline powder particles and no signs of brittle cracking (see below).

In the present work, we exploit the low temperature plasticity of the feedstock powder to prepare a dense bulk material with similar and unusual mechanical properties at low temperatures. The primary scope of this study is to report and discuss the observed high plasticity of this material at room temperature and at 77 K.

2. MATERIAL AND METHODS

The feedstock powder was prepared using atomization in argon by LERMPS/PERSEE company (France). The size distribution of spherical particles is characterized by d_{10} = 13.7 µm, d_{50} = 29.0 µm, d_{90} = 51.2 µm as determined by laser granulometry. The chemical analysis of Al, B and Zr in the atomized powder was performed by ICP-OES method using the Iris Intrepid HR, Thermo Scientific. Carbon content was determined by absorption spectrometer LECO CS-444. The oxygen analysis was performed using an absorption spectrometer LECO TC-300.

The atomized powder was consolidated using two different devices: SPS 10-4 apparatus (Thermal Technology LLC) and FCT HP D10 apparatus. Graphite foil was used to separate the SPS graphite tools (die and punches) with a diameter of 20 mm (50 mm for FCT apparatus) from the sintered powder. The graphite foil was later replaced by a tungsten foil, which successfully prevented contamination of the sintered sample by carbon. The powder in the die was heated to the sintering temperature of 1373 K (1273 K for FCT) with a heating

* Tel.: +420 2 21911362;
E-mail address: sima@met.mff.cuni.cz.

67   rate of 200 K/min (100 K/min for FCT). A pressure of 70 MPa (48 MPa for FCT) was applied
68   and maintained until completion of sintering. The dwell time at 1373 K (1273 K for FCT) was
69   3 min (30 min for FCT), followed by fast cooling (200 K/min) to 1123 K and then by slower
70   cooling (100 K/min) to room temperature. This choice of sintering parameters is close to the
71   SPS conditions used in [10]. The dimensions of the sintered cylindrical samples were Ø 19
72   mm x 5 mm (Ø 49 mm x 30 mm for FCT).

73   The microstructure and phase composition of the sintered samples were characterized by X-
74   ray diffraction (XRD), scanning electron microscopy (SEM) with electron backscatter
75   diffraction (EBSD) and by transmission electron microscopy (TEM). XRD measurements
76   were performed using a Bragg Brentano θ/2θ Bruker X-ray diffractometer, type D8 (Cu K_α
77   and Co $K_{\alpha 1}$ radiation). SEM observations were performed using Zeiss Auriga Compact
78   Crossbeam[®] microscope equipped with EDAX EBSD camera DigiView 5. The identification
79   and visualization of grains was made using the EBSD method by orientation imaging maps.
80   TEM specimens were prepared by mechanical grinding and polishing of thin targets to a
81   thickness of about 100 μm, and thinning to electron transparency using a Struers Tenupol 2
82   twin jet electrolytic polisher. TEM observations were performed using a JEOL 2000FX
83   electron microscope.

84   Mechanical properties of the feedstock powder were characterized using a Qness Q10A
85   microhardness tester with Vickers load of 25 gram. The same measurements were made on
86   sintered samples in different parts of cylindrical SPS discs, parallel and perpendicular to the
87   cylindrical axis. Cuboid-shaped compressive samples, typically of 4.9 x 3.5 x 3.5 mm^3, were
88   sectioned by diamond saw from the SPS disk parallel and perpendicular to the axis of the
89   disk. Samples for tensile tests with round cross-section (Ø4 mm) and threaded shoulders
90   were cut parallel to the axis of the bigger SPS-disk. The tests were performed in air at RT
91   and in liquid nitrogen at 77 K with an initial strain rate of 1.0 x 10^{-3} s^{-1}, using an Instron 1186
92   universal testing machine.

93   The elastic properties (Young's and shear moduli) of the examined material were measured
94   by a combination of two ultrasonic methods: the pulse-echo method [11] and the resonant
95   ultrasound spectroscopy [12,13]. For the ultrasonic measurements, a perfect cuboid sample
96   of dimensions approximately 2.0 x 3.0 x 4.5 mm^3 was used. Firstly, the velocities of
97   longitudinal and shear ultrasonic waves in three directions perpendicular to the faces of the
98   sample were measured at RT (295 K) using the pulse-echo (P-E) method in order to confirm
99   the assumed elastic isotropy of the compact. The outputs of the P-E method also enabled
100 direct calculation of the Young's modulus E and the shear modulus G. These values were
101 then used as initial approximations for the inverse procedure in the resonant ultrasound
102 spectroscopy (RUS) method. Secondly, the RUS method was applied to determine
103 accurately the elastic constants in the temperature range from RT to 80 K.

104
105 **3. RESULTS AND DISCUSSION**
106
107 **3.1.   Material characterization**

108 The results of the chemical analysis of the atomized powder are displayed in Table 1.

109

110

111 **Table 1. Chemical composition of the atomized powder (± standard deviation).**

* Tel.: +420 2 21911362;
E-mail address: sima@met.mff.cuni.cz.

element	Fe	Al	B	C	O	Zr
at.%	bal.	30.8 ± 0.2	0.109 ± 0.005	0.059 ± 0.001	0.132 ±0.003	0.355 ± 0.005

112

113　The XRD pattern (the red curve in Fig. 1) of the as-received atomized powder showed the
114　presence of the ordered B2 phase[1]. The Rietveld profile analysis of the XRD powder pattern
115　revealed about 0.6 wt.% of the $λ_1$ hexagonal C14 Laves phase in the atomized powder, in
116　agreement with former observations [14,15].
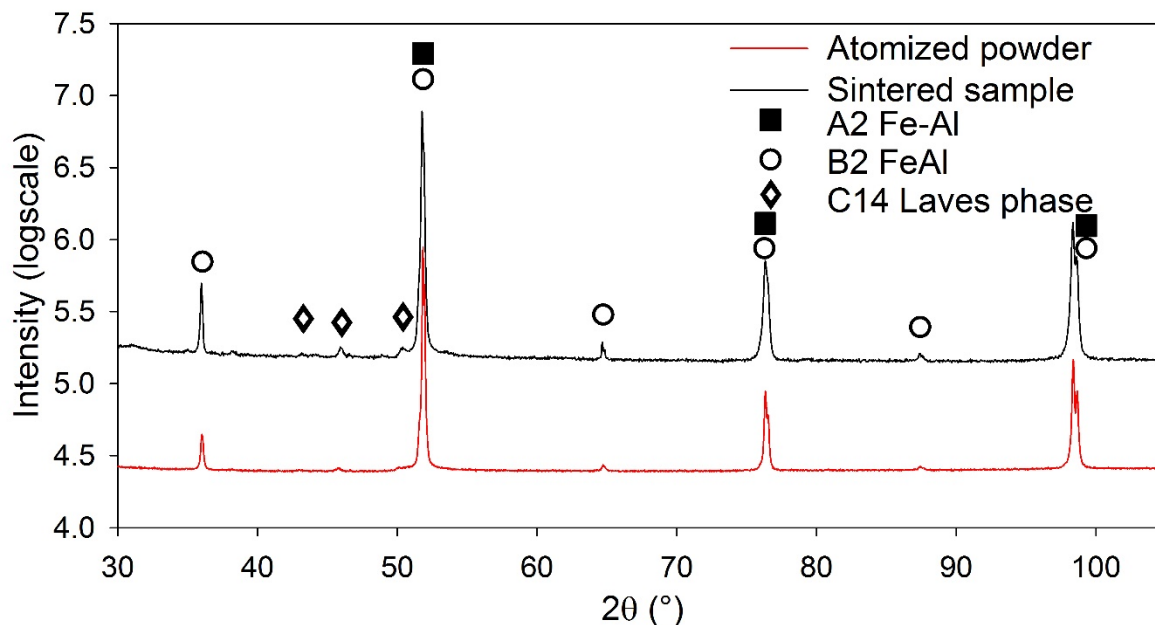
117

118　**Fig. 1. XRD patterns of the atomized powder and sintered sample.**

119

120　The microstructure of individual atomized powder particles was successfully determined by
121　SEM and EBSD methods (Fig. 2). Some of the particles have a spherical cavity inside (Fig. 2
122　below). These particles solidified with inside argon bubbles during atomization process.

123　The microstructure of atomized powder particles, which were mechanically activated by
124　milling at 77 K, is dramatically changed and shows clear signs of the intrinsic low
125　temperature plasticity (i.e. compressive and shear plastic strain) (Fig. 3). The milled powder
126　grains possess heavily strained and disordered A2 (bcc) crystal structure. The A2 crystal
127　structure of the cryomilled powder and the absence of the B2 long-range ordered phase
128　were confirmed also by XRD measurement.

---

[1] The fully developed $D0_3$ equilibrium structure with fcc Bravais lattice and doubled lattice
parameter (a = 0.57914(2) nm) was observed after annealing of the powder for 408 h at
693 K under an argon atmosphere.

* Tel.: +420 2 21911362;
E-mail address: sima@met.mff.cuni.cz.

129
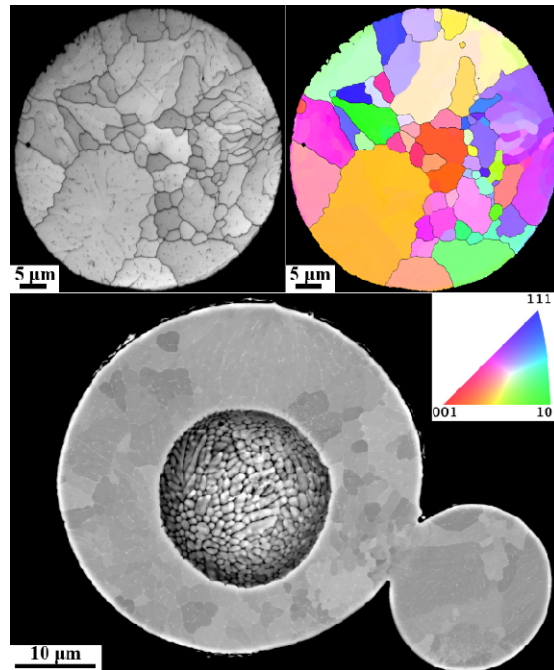
Fig. 2. The microstructure of an atomized powder particle observed by EBSD method (image quality map and orientation imaging map – upper images) and a particle with spherical cavity (SEM channeling contrast - bottom).

133

134
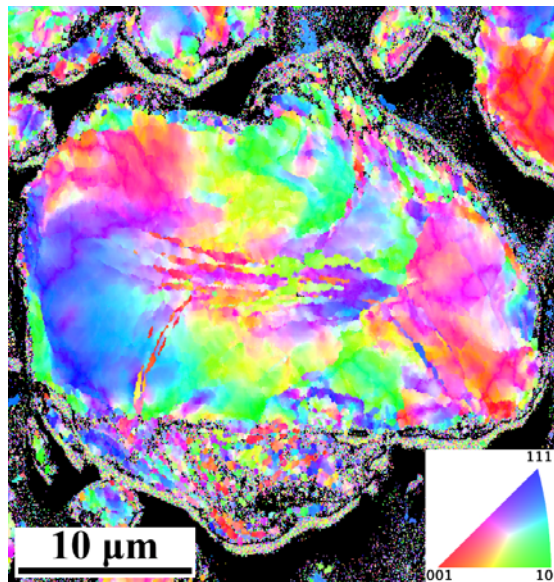
Fig. 3. Orientation imaging map of a cryo-milled (77 K) powder particle with the disordered A2 (bcc) structure.

Inspection of all sintered samples by electron microscopy revealed fully dense microstructure without any noticeable porosity. The sintered microstructure resembles the

* Tel.: +420 2 21911362;
E-mail address: sima@met.mff.cuni.cz.

139   microstructure of atomized particles with very similar grains of the ordered B2 structure (Fig.
140   4).

141

142
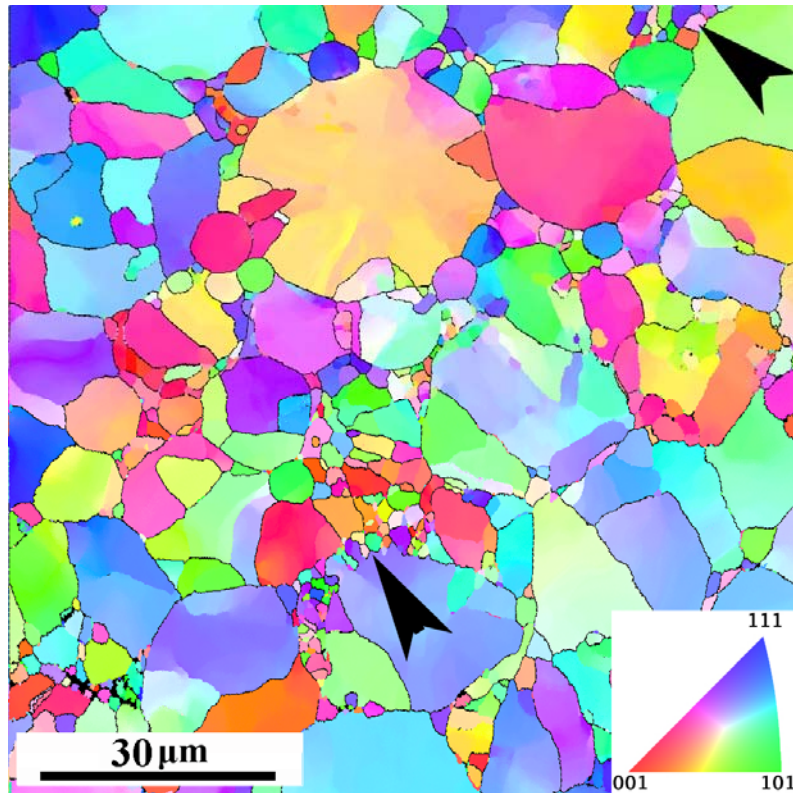
Fig. 4. Orientation imaging map of the sintered bulk material with the ordered B2 structure. The arrows point to regions with fine grains.

145

146   The sintered microstructure contains also regions with new fine grains (Fig. 4) filling up the
147   volume among original powder particles. The fine grains must have grown during the
148   sintering process. The resulting microstructure has therefore a bimodal or multimodal
149   distribution of grain sizes. XRD pattern of the sintered material (see Fig. 1) showed again the
150   presence of the ordered B2 phase with small amount of the λ_1 hexagonal C14 Laves phase.

151   Note that surface of several sintered samples was in contact with the graphite foil during the
152   SPS process. It resulted in the formation of κ-$Fe_3AlC_{0.5}$ carbide particles extending several
153   micrometers deep into the sintered material. Substitution of the graphite foil by the tungsten
154   foil fully prevented the formation of the carbide.

155

156   **3.2.   Deformation behavior**

* Tel.: +420 2 21911362;
E-mail address: sima@met.mff.cuni.cz.

157 Mechanical properties were studied using microhardness measurements at room
158 temperature (RT) and using both compression and tensile tests at RT and 77 K.

159 The results of all microhardness measurements are summarized in Table 2. As can be seen
160 from measured hardness values of SPS samples and their standard deviations, the bulk
161 material is homogeneous in the entire volume and the sintering process did not lead to a
162 measurable deviation from microhardness values of the feedstock powder particles.

163

164 **Table 2. Microhardness HV 0.025 of powder particles and sintered materials.**

	HV 0.025
atomized powder	380 ± 20
SPS bulk	370 ± 15

165

166 True stress vs logarithmic plastic strain curves are shown in Fig. 5, the yield strength,
167 maximum strength and logarithmic plastic strain values with their standard deviations are
168 summarized in Table 3.

169
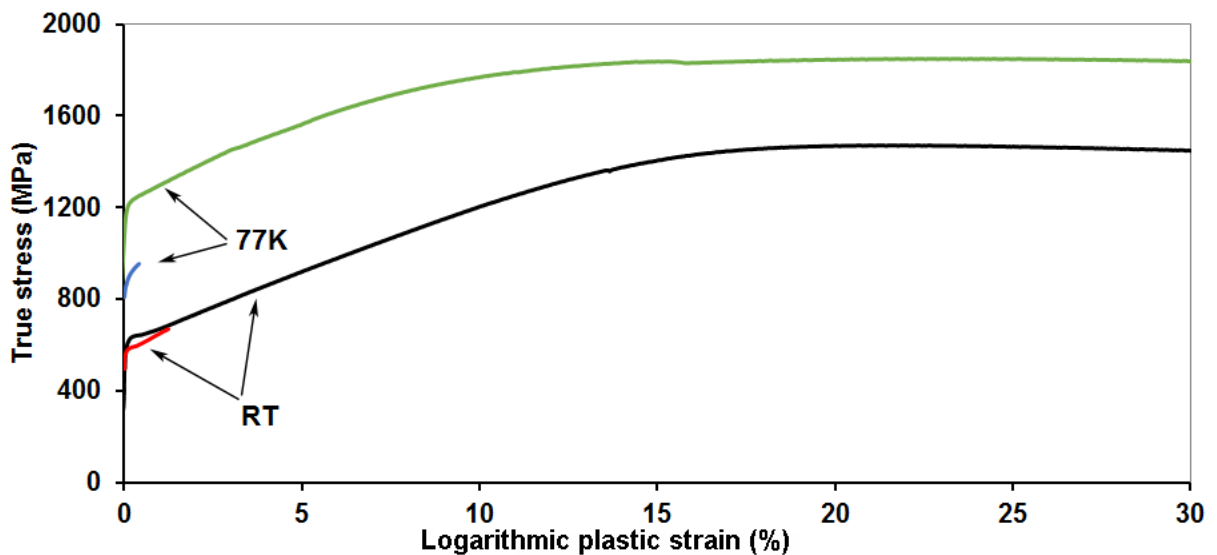
170

171 **Fig. 5. Compressive (black and green) and tensile (red and blue) true stress vs**
172 **logarithmic plastic strain curves for the sintered bulk material at RT and 77 K.**

173

174 The data in Table 3 represent behavior of four sets of three samples measured during
175 compressive and tensile tests in air at RT and in liquid nitrogen at 77 K, irrespective of how
176 they were cut from SPS samples.

177

* Tel.: +420 2 21911362;
E-mail address: sima@met.mff.cuni.cz.

178 **Table 3. The yield strength σ_{02}, maximum strength σ_{max} and logarithmic plastic strain**
179 **of the sintered bulk material in air at RT and in liquid nitrogen at 77 K.**

| Temperature	σ_{02} (MPa) (compression, tension)	σ_{max} (MPa) (compression, tension)	Plastic strain (%) (compression, tension)
RT	630 ± 10, 590 ± 10	1530 ± 60, 660 ± 10	> 30, 1.2 ± 0.1
77 K	1215 ± 15, 920 ± 10	1850 ± 10, 950 ± 10	> 30, 0.4 ± 0.1

180

181 Note the relatively very good reproducibility of all parameters in Table 3 showing stability of
182 the bulk material against variation of the SPS conditions. Substantial is the difference
183 between plasticity of the material in compression and in tension.

184

185 ### 3.3.   Dislocations in compression and fracture in tension

186 The transmission electron microscopy (Fig. 6) of the studied bulk material revealed the
187 following. In the as received material there is a very low dislocation density and a network of
188 λ_1 Laves phase particles in B2 matrix grains (Fig. 6a). The material after compressive test at
189 RT displays an inhomogeneous tangle of dislocations (Fig. 6b). Signs of recovery were
190 detected at higher magnifications, i.e. cells with low dislocation density surrounded by cell
191 walls with high density of dislocations with mostly identical Burgers vectors (see Fig. 7).
192 Dislocation tangles contain dislocations from several different slip systems forming a dense
193 network. The seemingly dislocation-free zone appearing as a gray band on the right side of
194 Fig. 6b is a diffraction contrast artefact that does not show the real dislocation structure of
195 the specimen. However, the material compressed at 77 K contains only high density of
196 homogeneously distributed dislocations with the exception of apparently non-deformed
197 particles (Fig. 6c).

198
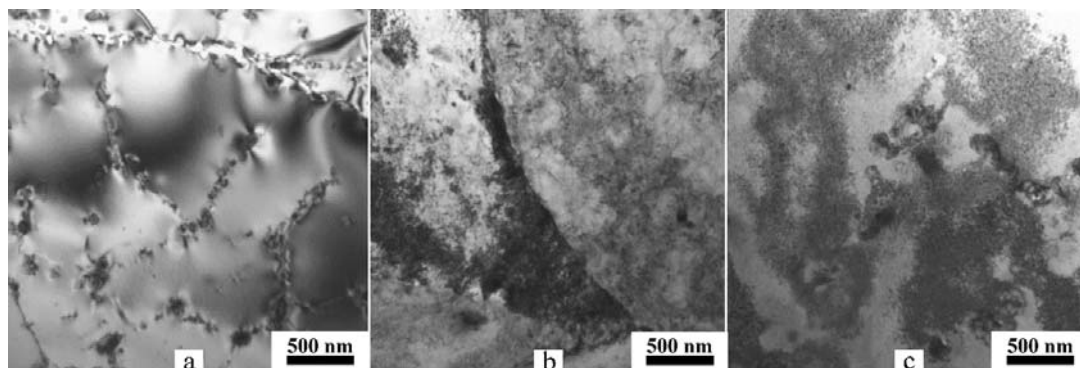
199

200

201 **Fig. 6. TEM images of the sintered material: (a) as received; (b) after compressive test**
202 **at RT; (c) after compressive test at 77 K.**

203

* Tel.: +420 2 21911362;
E-mail address: sima@met.mff.cuni.cz.

204 The SEM micrographs of the fracture surface after tensile test show that the fracture
205 occurred in a brittle manner with a nearly planar fracture surface that is perpendicular to the
206 applied tensile stress (Fig. 8). The fracture surface contains evidence of a combination of
207 interparticle and intergranular decohesion and also transgranular cleavage (Fig. 8).
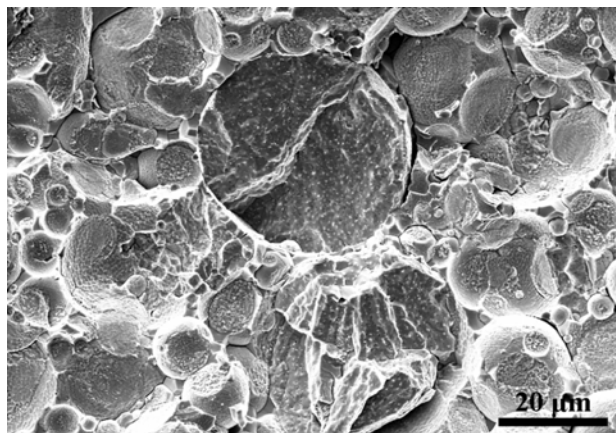
208
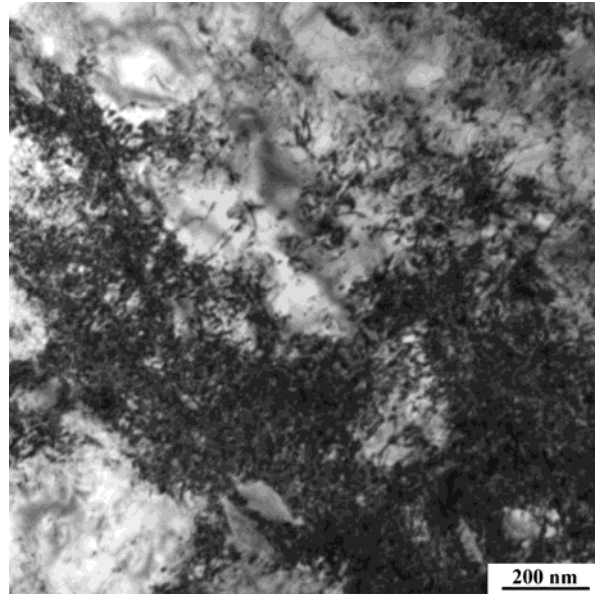
209

210

211 **Fig. 7. TEM image of the sintered material after compressive test at RT.**

212

213

214

215 **Fig. 8. SEM image of the fracture surface after tensile test at RT.**

216

* Tel.: +420 2 21911362;
E-mail address: sima@met.mff.cuni.cz.

217 **3.4.   Elastic moduli**

218   The density of the bulk material was determined from volume and mass of cuboid-shaped
219   samples and equals to 6290 ± 20 kg.m^{-3}. The density value together with a very good
220   transmission of ultrasonic wave through the samples, confirmed the homogeneity of the SPS
221   material and the absence of macroscopic defects and porosity. Ultrasound velocities were
222   determined by the pulse-echo method in three orthogonal directions. These three velocity
223   values did not mutually differ by more than 1.2 %, therefore the material is isotropic.

224   The RUS method is based on measurements of the resonant spectrum of free elastic
225   vibrations of the sample, from which the elastic constants are determined via an iterative
226   inverse procedure [12]. The temperature dependence of Young's modulus *E(T)* and shear
227   modulus *G(T)* is shown in Fig. 9. The elastic moduli data for temperatures of performed
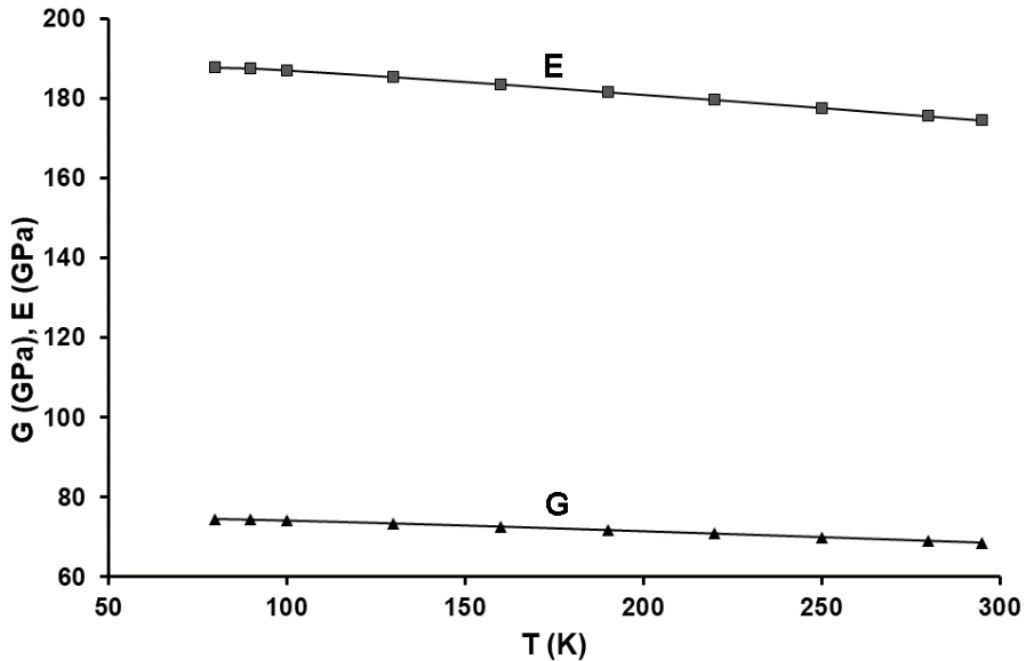228   deformation tests are shown in Table 4.

229

230

231

232   **Fig. 9. Temperature dependence of the Young's modulus *E* and shear modulus *G* of**
233   **the sintered material.**

234   Homogeneous isotropic linear elastic materials have their elastic properties uniquely
235   determined by two moduli. We calculated bulk modulus *B* according to the formula

$$B = \frac{EG}{3(3G - E)}$$

236

237   and the ratio *B/G*, introduced by Pugh [16] as a measure of ductility. If *B/G* > 1.75 the
238   material is expected to deform in a plastic manner, whereas the lower values of B/G are

* Tel.: +420 2 21911362;
E-mail address: sima@met.mff.cuni.cz.

239 associated with brittleness. Values of *B* and *B/G* for temperatures of performed deformation
240 tests are listed in Table 4.

241

242 **Table 4. Elastic moduli *E, G, B* and *B/G* of the sintered material at RT and 80 K.**

Temperature	*E* (GPa)	*G* (GPa)	*B* (GPa)	*B/G*
RT	174.4 ± 1.4	68.5 ± 0.3	128 ± 9	1.87 ± 0.12
80 K	187.7 ± 1.4	74.5 ± 0.3	132 ± 9	1.77 ± 0.12

243

244 The obtained data do not show any anomaly in the temperature dependence below RT. The
245 Young's modulus at RT for our sintered material is higher or close above the values obtained
246 in [17,18] for binary cast Fe-Al alloy with the same Al – concentration.

247

248 ### 3.5.   Discussion

249 The reason for different plasticity of our Fe-Al material in compression and in tension in air
250 can be probably found in the following facts:

251 1) The environmental embrittlement is often considered as a major cause for the low ductility
252 at RT in air [19]. It is related to high reactivity of Al atoms with the moisture in air. It creates
253 hydrogen that penetrates as atomic hydrogen into material and very probably reduces the
254 surface energy (the strength of interatomic bonds), which lowers the fracture toughness
255 [20,21].

256 However, it seems that the hydrogen embrittlement phenomenon does not influence the
257 deformation behavior of our material. It may be due to good passivation of the surface of
258 atomized particles that lowers hydrogen diffusivity in the sintered material. No ageing effect
259 or a degradation of the powder has been observed after nearly three years. The
260 improvement of plasticity in compression may be also due to the boron addition that
261 increases grain boundary strength. There may also be an effect of Zr containing λ_1 particles
262 or borides as observed in [2] for a material of nearly the same composition.

263 2) The poor plasticity in tension is not an intrinsic behavior of the alloy (see dominating role
264 of dislocation motion in compression), but it comes probably from nucleated
265 nano/microcracks between sintered powder particles and/or cavities in originally partly
266 hollow atomized particles. The microcracks open and propagate in the mode I (opening) in
267 tension. Assuming a microcrack nucleates at yielding in tension, the crack propagates
268 immediately after its nucleation when the stress for the crack propagation σ_f is lower than
269 the yield stress σ_y (fracture in a brittle manner). On the other hand, when $\sigma_y < \sigma_f$, the crack
270 propagation could occur only after additional plastic flow giving rise to work hardening,
271 indicating that fracture in tension could be delayed in regions with finer grain size on the
272 basis of the Hall-Petch relationship [22]. The finer grain size regions have higher local yield
273 strength and that may lead to increased ductility of the sintered sample. This effect was
274 observed in polycrystalline isostructural NiAl samples at 673 K [22].

275 The grain refinement can be achieved by milling of the iron aluminide powder, but this
276 procedure produces also a significant strain hardening of the milled particles. Their

* Tel.: +420 2 21911362;
E-mail address: sima@met.mff.cuni.cz.

microhardness increases according to our measurements typically by about 60% and this strain hardening also leads to the increase of the yield strength of the sintered compact material. However, the milling procedure destroys the passivated surface of atomized particles and then the environmental embrittlement of sintered material can be expected. It is therefore expected that a bulk material prepared from milled powder will have higher strength. On the other hand, such material will be probably also brittle not only in tension, but also in compression.

In case of our measurements in compression the propagation of nucleated or pre-existing nano/microcracks does not occur, the internal stress does not reach a critical value σ_f for a fracture in a brittle manner. The sample in compression has the capacity for plastic deformation and even for the plastic flow (see Fig. 5). After compression, the deformed sample has a typical barrel-shaped form.

3) The influence of temperature below RT on this behavior does not seem to be significant. The observed signs of dynamic recovery at RT only confirm the role of dislocations in compressive deformation. The measured shear modulus values scale with the resistance of the material to plastic deformation and relate this way to its hardness. The relative increase of the yield stress (in both tension and compression) due to the lowering of temperature is naturally higher than the relative increase of the shear modulus value. It is interesting that the corresponding absolute increase of the maximum flow stress σ_{max} in compression is the same as the increase of σ_{02} (and also σ_{max}) in tension. Pugh's values in Table 4 seem to be in agreement with observed plasticity in compression, but the application of this criterion to intermetallic compounds is probably less reliable than for pure metals.

4) Different slip directions in isostructural B2 alloys, the dislocation mobility, and related ductility/brittleness are in general a complex problem [23]. It was generally shown that an interplay of elastic anisotropy of these cubic materials, displacement vectors of metastable planar faults and their energies govern the choice of the activated slip directions [23,24].

4. CONCLUSION

Very good plasticity of the sintered FeAl-based material at both room temperature and 77 K has been evidenced by EBSD of the cryo-milled powder and in compression tests of the sintered material. The TEM observations confirm that dislocations enable the plastic flow in compression at low temperatures. The poor ductility in tension is not an intrinsic behavior of the alloy, but it results from the nucleation and opening of nano/microcracks between sintered powder particles and/or cavities in partly hollow atomized particles.

ACKNOWLEDGEMENTS

* Tel.: +420 2 21911362;
E-mail address: sima@met.mff.cuni.cz.

COMPETING INTERESTS

Authors have declared that no competing interests exist.

AUTHORS' CONTRIBUTIONS

All authors read and approved the final manuscript.

REFERENCES

1. Gaydosh DJ, Draper SL, Nathal MV. Microstructure and tensile properties of Fe-40 at. pct. Al alloys with C, Zr, Hf, and B additions. Metall Trans A. 1989;20A:1701-1713.

2. Morris DG, Morris-Muñoz MA. The influence of microstructure on the ductility of iron aluminides. Intermetallics. 1999;7:1121-1129.

3. Morris DG, Morris-Muñoz MA, Chao J. Development of high strength, high ductility and high creep resistant iron aluminide. Intermetallics. 2004;12:821-826.

4. Baker I. An overview of the mechanical properties of FeAl. Mater Res Soc Symp Proc. 2009;1128:1128-U02-01.

5. Zamanzade M, Barnoush A, Motz C. A review on the properties of iron aluminide intermetallics. Crystals. 2016;6:10. Available: http://dx.doi.org/10.3390/cryst6010010.

6. Orrù R, Licheri R, Locci AM, Cincotti A, Cao G. Consolidation/synthesis of materials by electric current activated/assisted sintering. Mater Sci Eng R. 2009;63:127-287.

7. Ji G, Bernard F, Launois S, Grosdidier T. Processing conditions, microstructure and mechanical properties of hetero-nanostructured ODS FeAl alloys produced by spark plasma sintering. Mater Sci Eng A. 2013;559:566-573.

8. Šíma V, Minárik P, Chráska T. Spark plasma sintering of ball milled and atomized powder based on Fe-Al. METAL 2015 – 24th International Conference on Metallurgy and Materials, Conference Proceedings. TANGER Ltd: 2015;1340-1345.

9. Šíma V, Cieslar M, Çelikyürek I, Torun O, Chráska T. Fully dense fine grained FeAl-based intermetallics prepared by spark plasma sintering method. In: Marquis F, editor. Proceedings of the 8th Pacific Rim International Congress on Advanced Materials and Processing (PRICM8). Wiley: 2013;361-368.

10. Skiba T, Haušild P, Karlík M, Vanmeensel K, Vleugels J. Mechanical properties of spark plasma sintered FeAl intermetallics. Intermetallics. 2010;18:1410-1414.

11. Every AG, Sachse W, editors. Dynamic methods for measuring the elastic properties of solids, Handbook of elastic properties of solids, liquids and gases. Volume I. San Diego: Academic Press; 2001.

12. Leisure RG, Willis FA. Resonant ultrasound spectroscopy. J Phys: Condens Matter. 1997;9:6001-6029.

* Tel.: +420 2 21911362;
E-mail address: sima@met.mff.cuni.cz.

358 13. Sedlák P, Seiner H, Zídek J, Janovská M, Landa M. Determination of all 21 independent
359 elastic coefficients of generally anisotropic solids by resonant ultrasound spectroscopy:
360 benchmark examples. Experimental Mechanics. 2014;54:1073-1085.

361 14. Morris DG, Gutierrez-Urrutia I, Muñoz-Morris MA. The high-temperature creep behavior
362 of an Fe-Al-Zr alloy strengthened by intermetallic precipitates. Scripta Mater. 2007;57:449-
363 452.

364 15. Stein F, Sauthoff G, Palm M. Phases and phase equilibria in the Fe-Al-Zr system. Z
365 Metallkd. 2004;94:469-485.

366 16. Pugh SF. Relations between the elastic moduli and the plastic properties of
367 polycrystalline pure metals. Phil Mag. 1954;45:823-843.

368 17. Köster W, Gödecke T. Physical measurements on iron-aluminium-alloys between 10 at.
369 percent and 50 at. percent Al. 4. The modulus of elasticity of the alloys. Z Metallkde.
370 1982;73:111-114.

371 18. Frutos E, Morris DG, Morris-Muñoz MA. Evaluation of elasic modulus and hardness of
372 Fe-Al base intermetallics by nano-indentation techniques. Intermetallics. 2013;38:1-3.

373 19. Liu CT, Lee EH, McKamey CG. An environmental effect as the major cause for room-
374 temperature embrittlement in FeAl. Scr Met. 1989;23:875-880.

375 20. Zamanzade M, Vehoff H, Barnoush A. Cr effect on hydrogen embrittlement of iron
376 aluminides. Acta Mater. 2014;64:210-223.

377 21. Yoo MH, Fu CL. Cleavage fracture of ordered intermetallic alloys. Mater Sci Eng A.
378 1992;153:470-478.

379 22. Schulson EM, Barker DR. A brittle to ductile transition in NiAl of a critical grain size. Scr
380 Met. 1983;17:519-522.

381 23. Lin Yi-Shen, Cak M, Paidar V, Vitek V. Why is the slip direction different in different B2
382 alloys?. Acta Mater. 2012;60:881-888.

383 24. Cao GH, Becker AT, Wu D, Chumbley LS, Lograsso TA, Russel AM, et al. Mechanical
384 properties and determination of slip systems of the B2 YZn intermetallic compound. Acta
385 Mater. 2010;58:4298-4304.

* Tel.: +420 2 21911362;
E-mail address: sima@met.mff.cuni.cz.